Dalton Transactions

ROYAL SOCIETY OF CHEMISTRY

PAPER

View Article Online
View Journal | View Issue

Cite this: *Dalton Trans.*, 2025, **54**, 6896

A bentonite/ZIF-8 derived ZnO photocatalyst for the effective elimination of a mixture of endocrine disruptors under simulated solar light: estrogenicity mitigation†

Pedro César Quero-Jiménez, [a] Aracely Hernández-Ramírez, [a] Giselle Gomes,[b] Jorge Luis Guzmán-Mar, [a] Daniele Maia-Bila[b] and Laura Hinojosa-Reyes *[a]

The hybrid bentonite/ZnO composites based on the metal–organic framework (MOF) ZIF-8 were synthesized by a microwave method using 2-methylimidazole and zinc nitrate, and incorporating natural bentonite (5, 15, and 25 wt%) followed by thermal treatment at 550 °C. The as-prepared materials were characterized for their crystal structure, morphology, composition, surface chemical states, textural and optical properties. The photocatalytic activity of the ZnO/bentonite composites was evaluated in the degradation of a mixture solution of endocrine disruptors (EDCs) (bisphenol A, propylparaben, and 17α-ethinylestradiol, 5 mg L^{-1} each) at pH = 7 under simulated solar light. The material characterization showed that incorporating bentonite into ZnO increased the specific surface area, facilitated the formation of oxygen vacancies, and decreased the recombination rate of e^-/h^+ pairs compared to ZnO. The solar photocatalytic activity revealed that bentonite 15 wt%/ZIF-8 derived ZnO composite showed enhanced photocatalytic activity compared to ZIF-8 derived ZnO, allowing the total degradation and 61.26% mineralization of the EDC mixture in 240 min. Furthermore, the effluent showed a decrease in estrogenic activity by the end of the photocatalytic process, with no by-products formed that present estrogenic activity. The bentonite/ZIF-8 derived ZnO composite is proposed as an alternative ZnO-based catalyst that effectively removes the EDC compounds from aqueous media.

Received 19th January 2025,
Accepted 18th March 2025

DOI: 10.1039/d5dt00154d

rsc.li/dalton

1. Introduction

Endocrine-disrupting chemicals (EDCs) have been frequently reported to be present in ambient samples and wastewater treatment plant effluents.[1–4] Bisphenol A (BPA) has shown adverse effects on animals and humans due to prolonged exposure.[5] Propylparaben (PPB) has been used as a pharmaceutical aid (antifungal) and preservative in food and cosmetics.[6] Parabens cause inhibition of the embryonic phase of *Danio rerio* through reactions with neural proteins.[7] The hormone 17α-ethinylestradiol (EE2) is commonly used as an oral contraceptive in livestock and animal reproduction and in treating certain diseases.[8] Thus, continuously introducing BPA, PPB, and EE2 into aquatic environments adversely affects this ecosystem.

The degradation and mineralization of these contaminants can be achieved through heterogeneous photocatalysis using semiconductor materials that are photoexcited with radiation equal to or greater than the bandgap energy (E_g). As a result, holes (h^+) created in the valence band (VB) can oxidize water molecules that are adsorbed on the semiconductor's surface and produce hydroxyl radicals ($HO^\bullet$) (2.80 V *vs.* NHE). In the meantime, superoxide radicals ($O_2^{\bullet-}$) can be generated when the excited electrons (e^-) in the conduction band (CB) react with O_2. ZnO is one of the most used semiconductors; however, it has some disadvantages, such as a high recombination rate of e^-/h^+ pairs, low quantum yield, low surface area, and poor pore distribution, which affect the photocatalytic process.[9,10] Zinc oxide has been synthesized through the thermal treatment of a MOF known as ZIF-8, which features a zeolite-like structure. MOFs offer versatile options for designing hierarchical porosity and unique metal oxide structures.[11–13] An α-Fe_2O_3/ZnO material derived from ZIF-8 was evaluated in methylene blue oxidation allowing its complete degradation in 150 min under UV-LED light.[13] In another

[a]*Universidad Autónoma de Nuevo León, Facultad de Ciencias Químicas, Av. Universidad S/N, Cd. Universitaria, San Nicolás de los Garza N.L, C.P. 66455, Mexico. E-mail: laura.hinojosary@uanl.edu.mx*

[b]*Universidade do Estado do Rio de Janeiro, Department of Sanitary and Environment Engineering, Rua São Francisco Xavier, 524, Maracanã, 20550-900 Rio de Janeiro, Brazil*

† Electronic supplementary information (ESI) available. See DOI: https://doi.org/10.1039/d5dt00154d

study, ZnO derived from ZIF-8 coupled to $BiVO_4$ removed 99.34% tetracycline under simulated solar radiation in 30 min.[12] By incorporating ZnO derived from ZIF-8 into CdS, methyl orange and ciprofloxacin removal was achieved under simulated solar light in 40 min.[11]

Additionally, minerals such as bentonite for preparing materials applicable to photocatalysis have been described, providing an enhanced surface area and stability.[14] In a previous work, a bentonite–$ZrTiO_4$ material incorporating 3, 9, and 12 wt% of bentonite was obtained by an ultrasonic-assisted sol–gel method followed by calcination at 400 °C for 12 h and evaluated in the photocatalytic degradation of rhodamine B dye under natural solar light.[15] Recently, the TiO_2/bentonite/α-Fe_2O_3 composite obtained by mixing TiO_2, bentonite, and hematite (16 : 4 : 1) was evaluated in carmine indigo dye degradation under fluorescent radiation.[16]

This work assessed for the first time the impact of adding natural bentonite on the photocatalytic efficiency of ZIF-8-derived ZnO to eliminate a mixture of EDCs (BPA, PPB, and EE2) under simulated sunlight. Furthermore, the *in vitro* YES (Yeast Estrogen Screen) assay previously applied for treatments such as UV/chlorine[17] and UV/H_2O_2[18] was used to demonstrate the reduction of estrogenicity and the suitability of water for discharge following this photocatalytic treatment.

2. Materials and methods

2.1 Chemicals and reagents

Bisphenol A (BPA, ≥99%), propylparaben (PPB, ≥99%), 17α-ethinylestradiol (EE2, 98%), zinc nitrate hexahydrate ($Zn(NO_3)_2{\cdot}6H_2O$, 98%), 2-methylimidazole (99%), sodium chloride (NaCl, ≥99%), *N*,*O*-bis(trimethylsilyl)trifluoroacetamide with trimethylchlorosilane (BSTFA–TMCS (1%)) and pyridine (≥99%) were purchased from Sigma-Aldrich. Ethanol (99.6%) and sodium acetate ($C_2H_3NaO_2$, 99.8%) were acquired from DEQ Corporation. Methanol (HPLC/spectrometry grade) and chloroform (HPLC/GC grade) were acquired from TEDIA. Acetone (HPLC/spectrometry grade) was purchased from JT Baker. Bentonite was provided by the Geominera del Centro Company, located in the Central Region of Cuba, and situated in the Remedio municipality, 44 km northeast of Villa Clara.

2.2 Material synthesis

The synthesis of ZIF-8 was carried out using a previously described method,[19] with some modifications. First, 0.68 g of zinc nitrate hexahydrate was dissolved in 10 mL of methanol (solution A). Next, 0.64 g of 2-methylimidazole ligand and 0.04 g of sodium acetate (deprotonation agent) were dissolved in 10 mL of methanol (solution B) for 10 min. Then, solution A was added dropwise to solution B under continuous stirring for 30 min. Afterward, the mixture was transferred to Teflon vials and placed in a microwave oven (CEM, Mars6, One Touch Technology), where the temperature was maintained at 120 °C for 30 min (800 W). Subsequently, the resulting white solid was centrifuged at 10 000 rpm for 5 min (Thermo Fisher Scientific, Servall ST16). Successively, the solid was washed with methanol and bidistilled water. Finally, the samples were dried in an oven at 80 °C for 12 h. ZnO was obtained from the thermal treatment of ZIF-8 at 550 °C for 6 h with a heating ramp of 2 °C min^{-1} under an air atmosphere. The bentonite-X wt%/ZnO composites were synthesized using the described ZIF-8 synthesis procedure, adding 0.10, 0.31, and 0.51 g of washed bentonite, corresponding to 5, 15, and 25 wt%, respectively, dispersed in 10 mL of methanol into solution B. Before the synthesis, the raw bentonite was sieved in a 100-mesh screen and activated in 3% Na_2CO_3 aqueous solution. The suspension was stirred for 24 h at room temperature. After activation, the suspension was allowed to settle for 24 h to remove impurities. The supernatant was decanted, and the clay fraction was centrifuged, dried at 105 °C, and ground into a fine powder for experimental use.[20]

Finally, the obtained materials were calcined at 550 °C for 6 h with a heating ramp of 2 °C min^{-1} under an air atmosphere. The obtained composites were named B5ZnO, B15ZnO, and B25ZnO, respectively.

2.3 Photocatalyst characterization

A Mettler Toledo TGA/SDTA 851 equipment was used to perform thermogravimetric (TGA) and differential thermal analysis (DTA) between 25 and 800 °C (10 °C min^{-1}) under N_2 flow. The materials were characterized using X-ray diffraction (XRD) with Cu-Kα radiation over a 2θ range of 5–80° at a step size of 0.5° s^{-1}. This analysis, conducted on a Bruker AXS diffractometer, evaluated their crystalline structures and phase composition. The crystallite size was calculated in the diffractograms using the Scherrer equation (eqn (1)) from the most intense peak.

$$D = \frac{k\lambda}{\beta \cos \theta} \quad (1)$$

where k is a constant associated with the crystal shape (commonly 0.89 for spherical crystals with cubic symmetry[21]), D represents the average crystallite size perpendicular to the diffracting planes, λ is the wavelength of the X-rays, and θ is the Bragg angle.

X-ray fluorescence analysis was performed on a powder contained in a plastic vessel, utilizing a Panalytical EPSILON 3-XL system. The analysis was conducted at an acceleration voltage of 10 kV, with a reading duration of 15 min. Fourier-transform infrared spectroscopy (FTIR) was used to analyze the materials at a 1 wt% concentration in KBr using a Shimadzu IR Prestige 21™ FTIR spectrophotometer from 4000 to 450 cm^{-1}. Textural properties were assessed using a Micromeritics ASAP 2020 analyzer at −196 °C, following 12 h of degassing at 200 °C. Scanning electron microscopy (SEM-EDAX JSM-6490LV JEOL) was employed to study the morphology, utilizing secondary electron mode at 20 kV. EDS INCA x-act, Oxford Instruments, a fully integrated EDS detector, performed elemental chemical analysis on the samples. A monochromated aluminum Kα source (1486.6 eV) at 12 kV was used in a K-Alpha Surface

Analysis system (Thermo Fisher Scientific) to conduct X-ray photoelectron spectroscopy (XPS) analysis. The materials' E_g was determined using the Kubelka–Munk function, derived from UV-Vis spectra obtained through diffuse reflectance spectroscopy conducted on an Ocean Optics USB 2000 spectrophotometer. Photoluminescence spectroscopy was carried out at room temperature on a PerkinElmer LS-55 system, recording the fluorescence emission in the 380–550 nm range with an excitation wavelength of 340 nm.

2.4 Photocatalytic activity of bentonite/ZIF-8-derived ZnO composites

Photocatalytic tests were performed to remove a mixture of BPA, PPB, and EE2 (5 mg L^{-1} each) using bentonite X wt%/ZIF-8-derived ZnO as catalysts. The experiments used a batch reactor with 0.5 g L^{-1} catalyst dosage and 150 mL of solution, stirred continuously under simulated sunlight provided by a solar simulator (SUNTEST, XLS+ Heraeus, Germany; 200–800 nm irradiation) for 240 min, with samples collected every 60 min. Before the experiments, the catalyst–solution mixture was kept in the dark for 60 min to achieve the adsorption–desorption equilibrium. Mineralization after 240 min was assessed by measuring total organic carbon (TOC, Shimadzu VCSN, China). The degradation of the contaminant mixture was monitored through gas chromatography with mass detection 5977B (GC-MS, Agilent Technologies, Santa Clara, CA, USA), as described in section S1 of the ESI.†

2.5 *In vitro* yeast estrogen screen (YES) assay

The estrogenic potential of the samples was assessed using the Yeast Estrogen Screen (YES) assay, an *in vitro* assay involving a recombinant reporter gene. This method, adapted from Routledge and Sumpter (1996)[22] and modified by Gomes *et al.* (2023),[23] activates the human estrogen receptor (hER) in *Saccharomyces cerevisiae* yeast when estrogenic substances are present. The activated receptor induces the lacZ gene, producing β-galactosidase, which breaks down chlorophenol red-β-D-galactopyranoside (CPRG) into chlorophenol red (CPR), resulting in a color change from yellow to red. Details of the procedure are described in section S2 of the ESI.†

2.6 Photocatalyst reusability study

The stability of the B15ZnO photocatalyst, which showed the best mineralization performance, was tested during three reuse cycles. After each cycle, the catalyst was separated by centrifugation (Thermo Scientific ST16) at 10 000 rpm for 15 min, washed with bidistilled water and ethanol, and dried at 85 °C for 12 h. Catalyst surfaces were examined using XRD and FTIR. Zinc leaching from the material was measured by atomic absorption spectroscopy (AAS) using a Varian SpectraA 220FS spectrophotometer.

2.7 Study of photogenerated reactive oxygen species (ROS) and charge carriers

A scavenger study explored the role of photocatalytically generated reactive oxygen species (ROS) and charge carriers. The reactive oxygen species $HO^{\bullet}$ and $O_2^{\bullet-}$ were evaluated using *tert*-butanol[24] and *p*-benzoquinone,[25,26] respectively. The role of h^+ was determined using formic acid.[27] To degrade the EDC mixture, 5 mmol L^{-1} of each tested scavenger was added in a 1 : 50 molar ratio, and the EDCs were analyzed by GC-MS in SIM mode.

3. Results and discussion

3.1 Photocatalyst characterization

The thermogravimetric analysis of ZIF-8 (Fig. 1Sa†) showed a first weight loss of approximately ~3% related to the evaporation of water and solvents retained in the material structure. At temperatures above 400 °C, a second weight loss (12.64%) occurred, associated with the transformation of ZIF-8 to ZnO, as evidenced by an exothermic peak in the DTA analysis of the material at 450 °C. At higher temperatures, the MOF showed a pronounced reduction in weight, attributed to the decomposition of the organic ligands in the material.[28] Similar results have been reported in previous studies.[29,30]

The TGA graph of the raw bentonite (Fig. 1Sb†) showed a first weight loss (14%) from 85 °C to 200 °C, which was related to the removal of physically adsorbed water on the material surface.[31] It coincided with the endothermic peak at 85 °C in the DTA curve. The material exhibited another weight loss (2.35%) from 405 to 500 °C, resulted in the formation of some metal oxides such as MgO.[32] Above 600 °C, another mass loss (1.61%) occurred, which was linked to the dehydroxylation of the silicate framework.[33]

Table 1 shows the chemical composition of natural and treated bentonite at 550 °C, determined by X-ray fluorescence analysis. Small amounts of TiO_2, V_2O_5, Cr_2O_3, MnO, and NiO (less than 2%) were present in the materials. In natural bentonite, ZnO (0.024%) and ZrO_2 (0.062%) were detected in addition to the oxides described above. It was observed that Fe_2O_3 was present at a high percentage (17.09% and 14.46% for natural and treated bentonite, respectively). These oxides could positively influence the degradation of the EDC mixture during the photocatalytic process.[34] Furthermore, Fe_2O_3 may add acidity to the composite surface, affecting contaminant adsorption and potentially enhancing the degradation efficiency.[16]

The diffractogram of natural bentonite (Fig. 2S†) showed that peaks at 2θ values of 19.75°, 27.95°, 35.02°, and 61.55° correspond to montmorillonite, while the peaks at 20.87° and 36.63° are reflections of SiO_2 and quartz, respectively, present in small quantities in the sample.[35] According to a previous study, the main mineralogical components of bentonite were montmorillonite (>90%), with small amounts of plagioclase, cristobalite, kaolinite, calcite, and quartz.[36] Fig. 1a displays the XRD patterns of the prepared materials, including calcined bentonite. The bentonite treated at 550 °C exhibited a diffractogram similar to natural bentonite, confirming its high thermal stability, as previously verified by thermogravimetric analysis. The XRD pattern of ZIF-8 confirmed the crystalline structure of the MOF, as shown in Fig. 1a. The diffractogram

Table 1 Chemical composition of the raw and calcined bentonite samples

Material	MgO	Al_2O_3	SiO_2	P_2O_5	SO_3	K_2O	CaO	TiO_2	V_2O_5	Cr_2O_3	MnO	Fe_2O_3	NiO	BaO	ZnO	ZrO_2
Raw bentonite	1.42	15.46	59.64	0.73	0.29	0.25	2.64	1.33	0.055	0.22	0.63	17.09	0.12	0.061	0.024	0.062
Calcined bentonite	1.55	16.35	61.96	0.59	0.22	0.24	2.37	1.19	0.047	0.20	0.53	14.56	0.099	0.083	—	—

Results are expressed as % by weight of oxide.

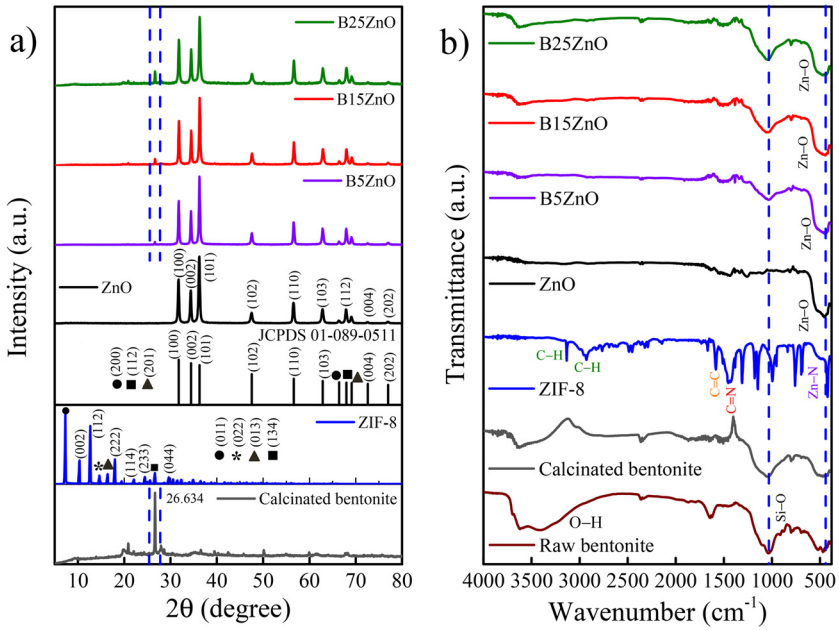

Fig. 1 (a) XRD and (b) FTIR analysis of natural bentonite, calcined bentonite, ZIF-8, ZIF-8-derived ZnO and the composites bentonite-*X*%/ZnO (*X* = 5, 15 and 25%).

displayed peaks at 2θ values of 7.32°, 10.35°, 12.68°, 14.65°, 16.42°, 17.99°, 21.08°, 24.43°, 26.63°, and 29.61°, corresponding to the planes (011), (002), (112), (022), (013), (222), (114), (233), (134), and (044), respectively.[28] The ZIF-8-derived ZnO showed peaks related to the wurtzite crystalline phase (JCPDS 01-089-0511).[37] In the case of the composites, the diffraction patterns presented peaks characteristic of ZnO derived from ZIF-8. In contrast, a small peak at 2θ = 26.60° corresponded to the most intense reflection of bentonite, which increases as the incorporation percentage of bentonite during the synthesis of ZIF-8 rises.

The crystallite size of bentonite decreased from 48.52 nm to 43.73 nm after calcination at 550 °C (see Table 2). The composite materials had a larger crystallite size than ZIF-8-derived ZnO, but their size decreased with increasing bentonite incorporation during synthesis. This is likely due to the prepared materials' larger surface area.

The FTIR spectra of the materials are shown in Fig. 1b. Natural bentonite displayed vibration bands at 3697.69, 3622.47, 3437.29, and 3221.26 cm^{-1} related to kaolinite, montmorillonite, water, and water strongly bound to the surface (or adsorbed) of the montmorillonite.[38] The peaks at 1635.70

Table 2 Values of crystallite size, surface area, pore size, and E_g of the materials

Material	Crystallite size[a] (nm)	Specific surface area ($m^2\ g^{-1}$)	Pore size (nm)	E_g (eV)	C content[b]
Raw bentonite	48.52	88.44	4.71	—	—
Calcined bentonite	43.73	68.64	5.79	—	14.24
ZIF-8	50.59	1399.67	2.11	—	70.53
ZnO	24.45	7.88	15.06	3.22	23.37
Bentonite-5%/ZnO	31.61	10.03	13.31	3.23	—
Bentonite-15%/ZnO	26.76	24.65	9.86	3.24	24.58
Bentonite-25%/ZnO	25.27	27.67	14.98	3.25	—

[a] The XRD plane in parentheses corresponds to the most intense peak to estimate the crystallite size. [b] Content determined by XPS analysis.

and 1033.88 cm^{-1} were related to the deformation vibration of water between octahedral layers and the Si–O vibration. Other low-intensity bands at 1093.56 and 798.56 cm^{-1} confirmed the presence of Si–O in the quartz structure. Additionally, bands corresponding to the Si–O–Mg and Si–O–Al bonds were observed at 692.47 and 518.87 cm^{-1}.[39]

The FTIR spectrum of ZIF-8 showed two bands at 3134.26 and 2929.87 cm^{-1}, corresponding to the symmetric C–H stretching.[28] The material also exhibited the C=N stretching vibration bands at 1585.48 and 1444.68 cm^{-1}. Bands produced by in-plane bending movements within the imidazole ring were observed between 1350 and 950 cm^{-1}. At 759.95 cm^{-1}, the characteristic band for out-of-plane bending movements of the imidazole ring was observed. The vibration band at 420.48 cm^{-1} was related to the Zn–N stretching of ZIF-8.[40] In ZnO, the FTIR spectrum displayed a strong band at 451.34 cm^{-1}, associated with the Zn–O stretching vibration.[41] For the synthesized composites (B5ZnO, B15ZnO, and B25ZnO), a band at 3630.03 cm^{-1} attributed to the presence of montmorillonite and adsorbed water (O–H stretching) on the surface of the materials was observed. These materials also showed a band at 1035.82 cm^{-1}, related to the Si–O vibration from bentonite; this band increased in intensity with the increased percentage of bentonite incorporated during the synthesis of ZIF-8. Furthermore, an intense band at 443.62 cm^{-1} from Zn–O stretching vibration was observed.

Nitrogen physisorption analyses revealed the textural properties of the obtained materials (Fig. 3S†). The natural and thermally treated bentonite at 550 °C exhibited specific surface area values of 88.44 and 68.64 $m^2\ g^{-1}$, respectively, with type IV adsorption isotherms, characteristic of mesoporous materials. Table 2 shows that the thermal treatment at 550 °C decreased the surface area of bentonite due to the collapse of the layered structure, confirmed by thermogravimetric analysis, which indicated a weight loss of 19.3%. In the case of ZIF-8, it presented a type I adsorption isotherm corresponding to a microporous material (2.11 nm) with a high surface area (1399.67 $m^2\ g^{-1}$),[41] which was transformed into ZnO (7.88 $m^2\ g^{-1}$) upon thermal treatment at 550 °C, as confirmed by XRD and FTIR studies (Fig. 1). During the synthesis of ZIF-8, an increase in bentonite led to a rise in the composite materials' surface area from 10.03 to 27.67 $m^2\ g^{-1}$, as shown in Table 2.

The SEM images of the materials are shown in Fig. 2. Bentonite showed irregular sheet morphology (Fig. 2a), according to a previous study.[42] However, during thermal treatment at 550 °C, the bentonite morphology collapsed into a more compact structure (Fig. 2b), decreasing its surface area (Table 2). In Fig. 2c, ZIF-8 presented a rhombic dodecahedron

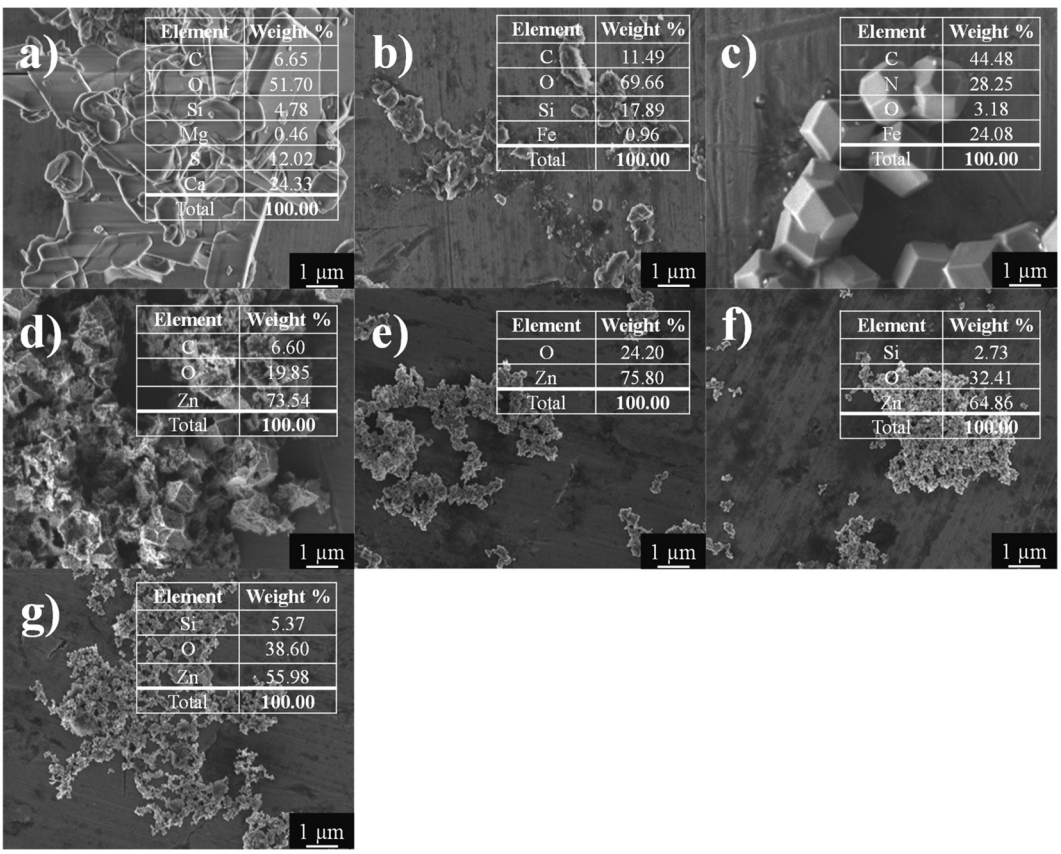

Fig. 2 SEM images and EDS analysis of (a) bentonite, (b) calcined bentonite, (c) ZIF-8, (d) ZIF-8-derived ZnO, (e) B5ZnO, (f) B15ZnO and (g) B25ZnO.

with a smooth surface and truncated corners featuring hexagonal face morphology, consistent with the recently reported study.[41] In the case of ZnO derived from ZIF-8, this material exhibits a morphology similar to the ZIF-8 precursor. However, the structure was contracted due to thermal treatment increasing the pore size from 2.11 to 15.06 nm (Table 2). These results aligned with previous studies where ZIF-8 obtained *via* a hydrothermal route was calcined at 500 °C for 2 h.[43] In the composites (Fig. 2e, f and g), a morphology similar to that of ZnO was observed, intercalating with bentonite sheets, particularly noted in the B25ZnO material.

According to the EDS analysis, natural bentonite contained C, O, Si, Mg, S, and Ca elements.[36] In the case of calcined bentonite, only C, O, Si, and Fe were detected. For ZIF-8, Zn of the metallic center of the MOF and C, O, and N, which comprise the binding agent 2-methylimidazole, were detected. For the bentonite-X wt%/ZnO materials, Zn and O were present. Si was also detected in materials with 15 and 25% incorporated bentonite, increasing from 2.73% to 5.37% wt.

The XPS full scan spectra of the individual materials and the B15ZnO composite are shown in Fig. 4S,† confirming the presence of the elements in the synthesized materials. The deconvolution of the Zn region in ZIF-8 (Fig. 3a) showed two peaks at 1044.28 eV (Zn $2p_{1/2}$) and 1021.28 eV (Zn $2p_{3/2}$).[44] A small peak at 1022.98 eV indicated the presence of the Zn–O/Zn–OH bond.[45] This peak results from the partial hydrolysis of ZIF-8 due to a water molecule attack. The Zn–N coordination bond in ZIF-8 partially decomposes during hydrolysis. First, the bond to the 2-methylimidazole ligand breaks, and subsequently, a hydroxyl is coordinated to zinc and a proton to the nitrogen in the ligand, resulting in an increase in the oxygen content due to the formation of a Zn–O bond.[46] In the Zn 2p spectra of ZIF-8-derived ZnO, two peaks were observed at 1044.18 eV (Zn $2p_{1/2}$) and 1021.08 eV (Zn $2p_{3/2}$), which correspond to the oxidation state Zn^{2+}.[47] Additionally, the peak corresponding to Zn $2p_{3/2}$ was deconvoluted into two signals at 1021.68 eV and 1020.88 eV, which can be attributed to the Zn–O–Zn and Zn–O bonds on the surface of the material.[48] In the case of the B15ZnO material, the peaks corresponding to Zn $2p_{1/2}$ and Zn $2p_{3/2}$ shifted towards higher binding energy values compared to ZnO, suggesting a decrease in the electron density of Zn in the composite acting as the electron donor.[11] This can be attributed to the surface-binding interaction between ZnO and metal oxides in bentonite, which causes electron transfer from ZnO to these species.[49]

The O 1s spectrum in ZIF-8 (Fig. 3b) showed a peak at 531.18 eV, which was deconvoluted into two peaks located at 531.08 and 532.18 eV, associated with the C–O and –OH/C–O–C bonds, respectively.[50] The peaks in the deconvoluted O 1s spectrum of bentonite corresponded to the O–M bond (532.08 eV) and O^{2-} (531.18 eV).[51] The deconvolution of the O 1s region in ZnO presented two peaks at 529.88 eV (O–Zn) and 531.38 eV (oxygen vacancies), formed because of thermal treatment.[11,52] These peaks slightly shifted towards higher binding energy values due to the decrease in the electron cloud density near these bonds. This effect is caused by incorporating bentonite into the material, which increases the oxygen vacancies or defects.[53] Thus, incorporating bentonite into the ZnO lattice increased the peak intensity of oxygen vacancies to 49.05% of the atomic percentage compared to 44.39% for ZnO. This indicated that the composite exhibited more oxygen defects than ZnO. These oxygen vacancies play a

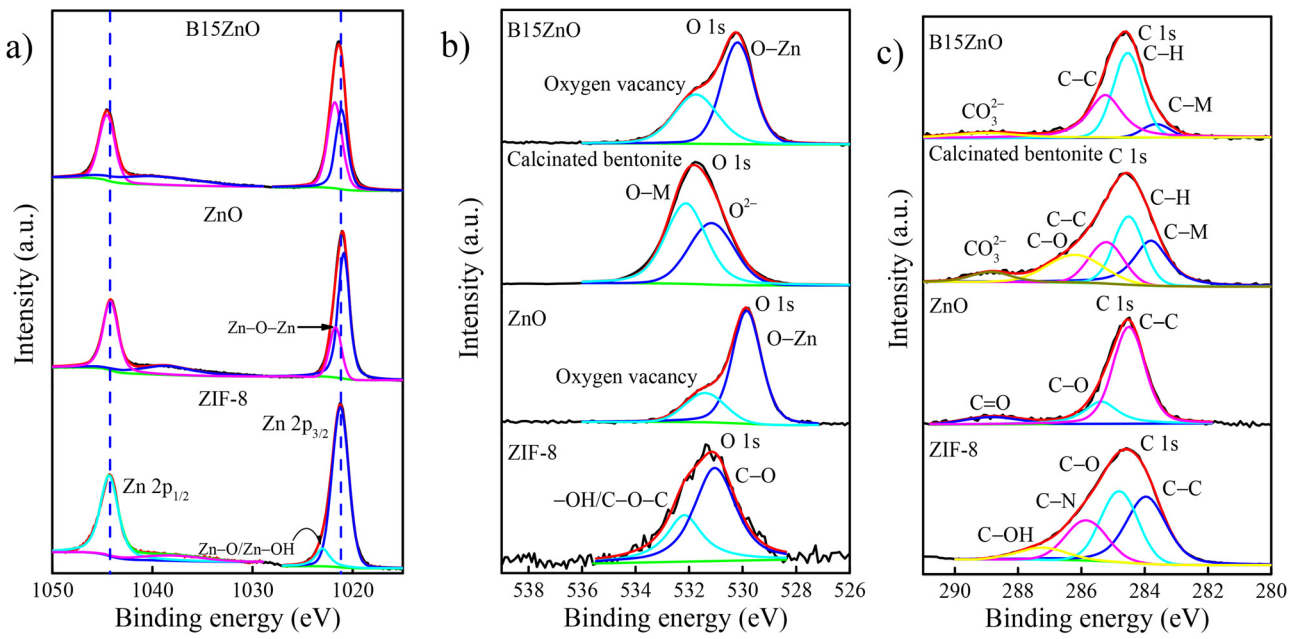

Fig. 3 High-resolution XPS spectra of (a) Zn 2p for ZIF-8, ZIF-8-derived ZnO and B15ZnO, and (b) O 1s and (c) C 1s for ZIF-8, ZIF-8-derived ZnO, calcined bentonite and B15ZnO.

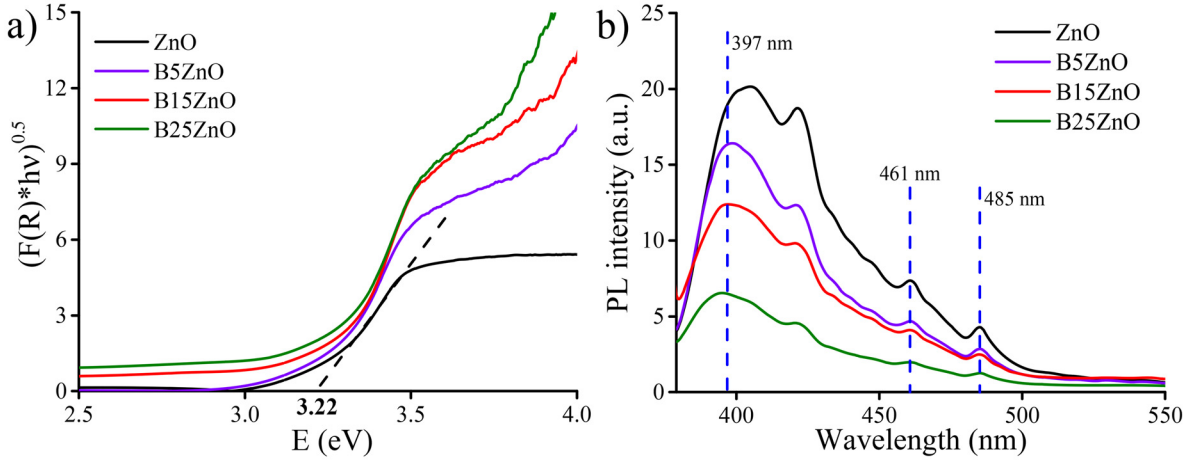

Fig. 4 (a) The Kubelka–Munk function $F(R)$ *vs.* energy (eV) and (b) photoluminescence spectra of the synthesized materials.

crucial role in enhancing the photocatalytic performance.[11,54] The deconvolution of the C 1s region in ZIF-8 (Fig. 3c) showed peaks at 283.98, 284.78, 285.88, and 287.28 eV, corresponding to the C–C, C–O, C–N, and C–OH bonds, respectively.[55] In the case of ZnO, two peaks were found at 284.48 and 285.38 eV, corresponding to the C–C, C–O, and C═O bonds.[52] The XPS analysis of the C 1s region of calcined bentonite showed peaks at binding energies of 283.78, 284.48, 285.18, 286.18, and 288.88 eV, related to C–metal, C–H, C–C, C–O, and CO_3^{2-} bonds, respectively.[56] In the composite, the peaks observed at 283.68, 284.58, 285.28, and 288.98 eV correspond to the C–metal, C–H, C–C, and CO_3^{2-} bonds, respectively. The C-metal signal peak could be related to carbon doping into ZnO and other metal oxides identified in bentonite.[57]

The N 1s spectrum (398.48 eV) in ZIF-8 (Fig. 5S†) was deconvoluted into two peaks located at 398.38 and 399.38 eV corresponding to the N–Zn bond,[45] and N═C bond.[55] The N 1s XPS spectrum with a low signal-to-noise ratio was observed in the B15ZnO sample. The fitted peak at 399.7 eV was related to the nitrogen species in the N–Zn–O bond, which confirmed the doping of nitrogen atoms into the ZnO lattice.[47]

The E_g values of the synthesized photocatalysts were calculated from the Tauc plots (Fig. 4a). The E_g of ZnO derived from ZIF-8 was 3.22 eV, higher than the values reported (3.10 eV).[12] The bentonite incorporated during the ZIF-8 synthesis did not modify the E_g values of the composites (3.23–3.25 eV, Table 2). The montmorillonite–TiO_2 composite prepared using a 10 : 1 (montmorillonite : TiO_2) ratio showed that montmorillonite slightly modified the E_g value of TiO_2 from 3.12 to 3.04 eV in the composite material.[58]

Fig. 4b shows the photoluminescence spectra of the prepared materials in the 380–550 nm range. The broad peak observed at approximately 397 nm results from the direct recombination of the free excitons. The blue-green luminescence at 461 and 485 nm arises from the radiative recombination of the photogenerated h^+ with the e^- trapped by the oxygen vacancies. Incorporating bentonite into ZIF-8-derived ZnO reduced the photoluminescence intensity of the composites compared to pure ZnO. This result indicated that the bentonite/ZnO materials present a lower e^-/h^+ recombination rate than ZnO, attributed to the increased surface oxygen vacancy defects.[54,59]

3.2 Photocatalytic activity evaluation of bentonite/ZnO

Materials prepared from the incorporation of 5, 15, and 25 wt% natural bentonite during the synthesis of ZIF-8 and subsequent calcination at 550 °C were evaluated in the degradation of the PPB, BPA, and EE2 mixture (5 mg L^{-1}, each) under simulated solar light for 240 min.

3.2.1 Effect of pH on the photocatalytic degradation of the EDC mixture. The effect of solution pH in the range of 4 to 10 on the photocatalytic degradation of the PPB, BPA, and EE2 mixture using B15ZnO materials was evaluated. The pH of the contaminant solution influenced the surface charge of the photocatalyst.[60] Fig. 5a shows that the degradation was enhanced at pH = 7 (neutral) compared with the results at pH 4 and 10, achieving the highest mineralization (61.26%) and degradation (86.42% (PPB), 72.47% (BPA), and 98.63% (EE2)). It has been reported that the pzc (point of zero charge) for ZnO is 9.2.[61] In contrast, the reported value for the bentonite–ZnO composite prepared by the precipitation method using $ZnCl_2$ as an inorganic precursor and montmorillonite was 8.4,[62] so the degradation of the EDC mixture is favored at neutral pH because the catalyst's surface was positively charged.[63] On the other hand, the PPB (pK_a = 8.5), BPA (pK_a = 9.8–10.4), and EE2 (pK_a = 10.33) molecules exist in a non-dissociated form at pH = 7. Thus, adsorption is favored at a pH value lower than the pK_a of the EDCs, where the photocatalyst surface is positively charged. On the other hand, at pH values higher than pzc (pH > pzc), the ZnO surface is negatively charged, increasing the repulsion between the pollutant molecules and the catalyst particles, and decreasing the photocatalytic efficiency.[64]

3.2.2 Effect of bentonite incorporated into ZnO and control test for the photocatalytic elimination of the EDC mixture. The photocatalytic experiments with ZIF-8-derived

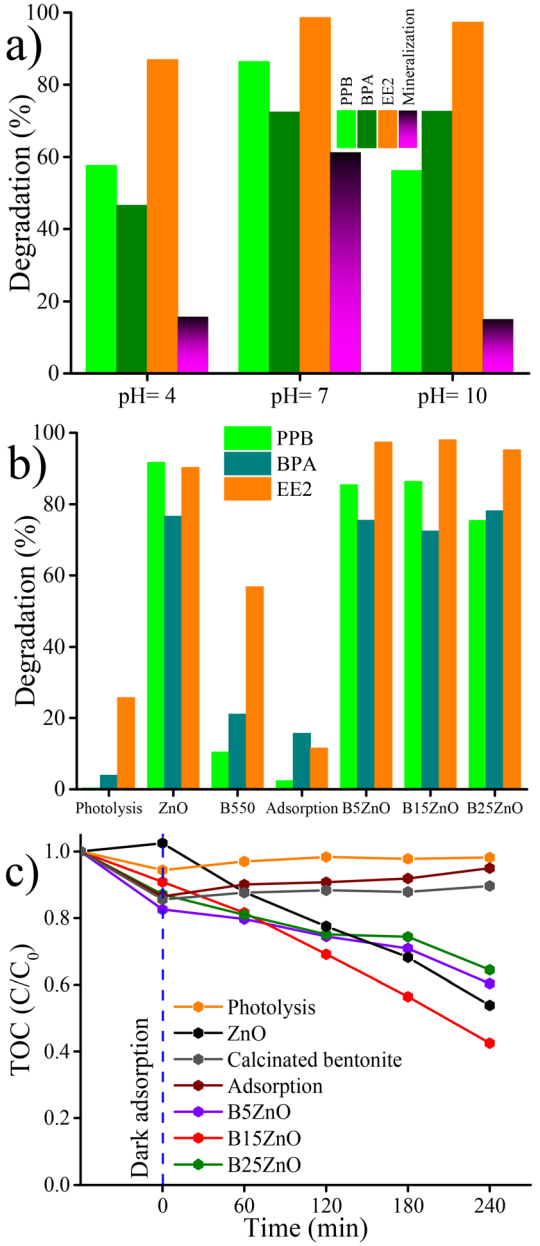

Fig. 5 (a) Effect of pH on the photocatalytic performance of B15ZnO, and (b) degradation and (c) mineralization of the EDC mixture by photolysis, adsorption, and photocatalysis with ZIF-8-derived ZnO, calcined bentonite, and the composite materials (0.5 g L^{-1} of catalyst, 5 mg L^{-1} of the PPB, BPA, and EE2 mixture at pH = 7).

ZnO incorporating 5, 15, and 25 wt% of bentonite for the degradation of the EDC mixture (Fig. 5b) showed that the B5ZnO material exhibited slightly higher activity (PPB: 85.45%, BPA: 75.51%, and EE2: 97.38%) compared to B15ZnO (PPB: 86.42%, BPA: 72.47%, and EE2: 98.03%) and B25ZnO (PPB: 75.46%, BPA: 78.14%, and EE2: 95.26%) composites. For the control tests, degradation values with ZnO (PPB: 91.77%, BPA: 76.62%, and EE2: 90.32%), treated bentonite at 550 °C (PPB: 10.46%, BPA: 21.10%, and EE2: 56.80%), photolysis (PPB: 0.3549%, BPA: 3.92%, and EE2: 25.74%), and adsorption (PPB: 2.39%, BPA: 15.70%, and EE2: 11.58%) were lower than the results observed by photocatalysis. In previous studies, the Gd_2WO_6/ZnO supported on 15% bentonite synthesized by a hydrothermal procedure showed the highest degradation efficiency in ciprofloxacin and bisphenol A, allowing 97.9 and 98.3%, respectively, within 60 min.[65]

The TOC abatement of the EDC mixture (Fig. 5c) showed that the highest mineralization was exhibited using the B15ZnO composite (61.26%), which may be related to the low photoluminescence intensity, indicative of a low e^-/h^+ pair recombination rate. Compared to B15ZnO, lower percentages of mineralization were obtained with B5ZnO and B25ZnO materials, 39.63% and 25.62%, respectively. On the other hand, the TOC removal values for ZnO, bentonite treated at 550 °C, and the photolysis and adsorption processes were 50.94%, 11.00%, 5.84%, and 19.27%, respectively. The high mineralization percentage exhibited by the B15ZnO composite can be related to a low-toxicity effluent.[66]

3.3 Photocatalytic pathway degradation of the EDC mixture solution using B15ZnO

The intermediates generated during the degradation of the EDC solution at pH = 7 using the B15ZnO material were identified through GC-MS analysis, as shown in Fig. 6. During PPB degradation, compound **I** (*m*/*z* 210.04) was detected, whose detection may be related to intramolecular coupling at high concentrations.[67] Compounds **II** (*m*/*z* 120.04) and **III** (*m*/*z* 210.04) were also detected, possibly due to radical attacks. In

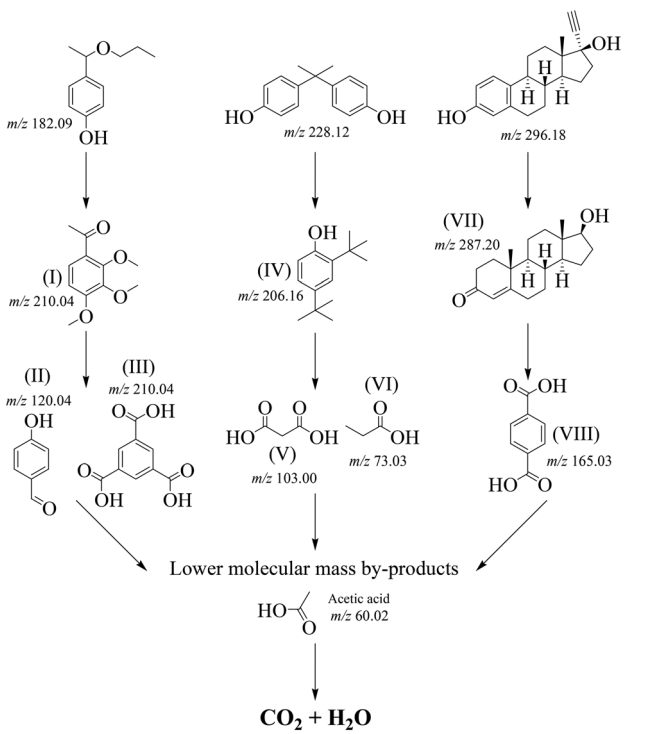

Fig. 6 Photocatalytic pathway degradation of the PPB, BPA and EE2 mixture solution using B15ZnO at pH = 7.

the degradation of BPA, 2,4-di-*tert*-butyl phenol (**IV**, *m*/*z* 206.16) was detected, which has been previously identified in the photocatalytic degradation of this pollutant.[68] Another by-product identified was malonic acid (**V**, *m*/*z* 103.00) and propionic acid (**VI**, *m*/*z* 73.03), which may form from the attack of the HO$^{\bullet}$ radical on the bond of the benzene ring and the C–C bonds between the isopropyl and benzene ring.[69] For EE2, testosterone by-product (**VII**, *m*/*z* 287.20) was identified, indicating the oxidation of the phenolic group in EE2.[70] The detection of terephthalic acid (**VIII**, *m*/*z* 165.03) indicates the breakdown of the hormone's structure as a result of radical-induced cleavage. During the degradation of the three EDCs, acetic acid (*m*/*z* 62.02) was observed, indicating the opening of the aromatic rings and the formation of lower molecular weight by-products.

3.4 Estrogenicity mitigation evaluation using the YES assay

The estrogenic activity of a mixture containing PPB, BPA, and EE2 was evaluated through photolysis, adsorption, and photocatalysis with B15ZnO and ZnO catalysts. The estrogenic activity was measured using the YES assay and expressed as estradiol equivalents (E2-EQ in ng L^{-1}). Fig. 6S† presents the positive control (E2) and negative control (Milli-Q water) curves. The results are shown as E2-EQ (Fig. 7).

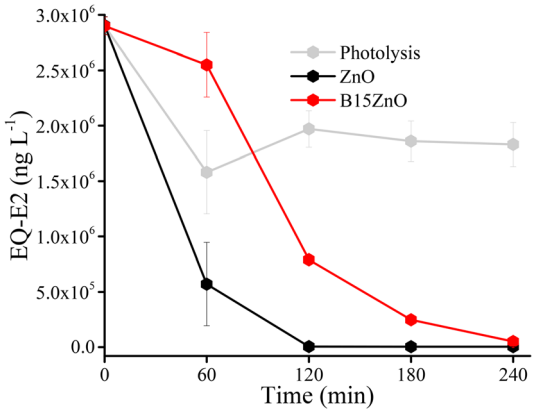

Fig. 7 Estrogenic mitigation (E2-EQ) during photocatalytic treatment using B15ZnO and the controls ZIF-8-derived ZnO and photolysis, up to 4 h of reaction (*n* = 2 replicates).

The E2-EQ of the aqueous mixture of EDCs (5 mg L^{-1} each) was 2.90 × 10^{6} ± 8.07 × 10^{4} ng L^{-1}. In the *in vitro* YES assay, the estrogenic response of each compound in the mixture can be expressed in relative potency, which reflects the affinity of each compound for the human estrogen receptor (ER).[23] In this context, PPB, BPA, and EE2 compounds showed relative potencies of 5.3 × 10^{-5}, 8 × 10^{-4}, and 1.15, respectively. These values indicate that EE2 has a high affinity for the ER, which explains its higher relative potency in the YES assay. PPB and BPA, although having low affinity for the nuclear ER compared to EE2, still contribute to the estrogenic activity of the mixture. The compounds' mechanism of action can explain the ER's affinity. The low relative potency of BPA can be attributed to its specific mechanism of action, which predominantly involves non-genomic pathways.[23] This characteristic limits its interaction with the nuclear estrogen receptor utilized in the YES assay, as BPA exhibits a notably low binding affinity for this receptor.[71,72]

The estrogenic activity results indicated that adsorption is not the primary mechanism for the removal of EDCs in the investigated catalysts, as this process reduced the E2-EQ value by approximately 10% for all the catalysts used (B15ZnO and ZnO derived from ZIF-8 catalysts). Regarding photolysis, a reduction of about 36% in the estrogenic activity of the mixture was observed, with the activity remaining constant after 120 min. These data are consistent with the degradation results of PPB, BPA, and EE2 obtained after 4 h of photolysis (PPB: 0.3549%, BPA: 3.92%, and EE2: 25.74%). As shown in Fig. 8, during the photocatalytic process using ZnO, the estrogenic activity of the mixture was reduced to E2-EQ values below the detection limit of the YES assay (LOD = 25.7 ± 2 ng L^{-1}) after 180 min of reaction. In the case of B15ZnO, estrogenic activity was significantly reduced, achieving a 98% reduction in E2-EQ values. Furthermore, based on the degra-

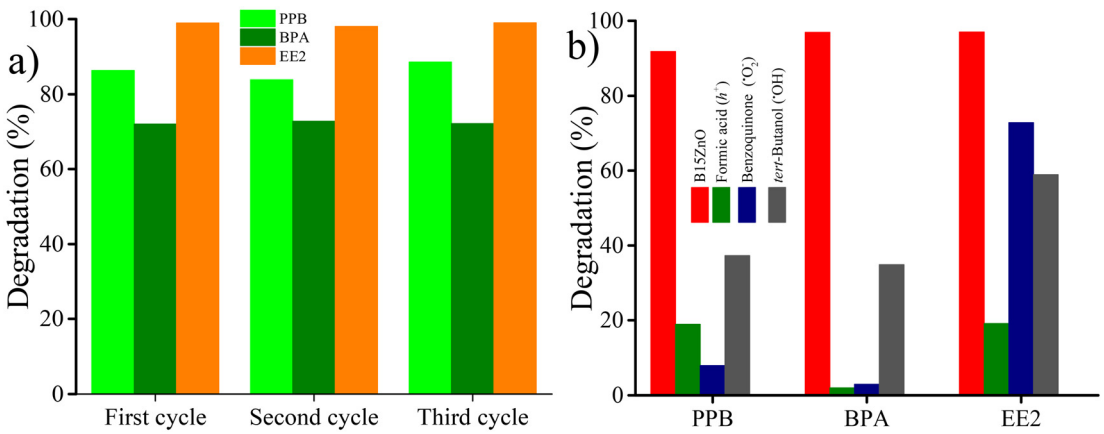

Fig. 8 (a) B15ZnO reusability study during three cycles, and (b) EDC mixture degradation using B15ZnO in the presence of scavengers under simulated solar light.

dation results of the mixture's compounds for this catalyst (PPB: 86.42%, BPA: 72.47%, and EE2: 98.63%), it was observed that the reduction in estrogenic activity after treatment with B15ZnO resulted from the degradation of the compounds and the absence of estrogenic by-products.

Previous studies have shown that other treatments, such as UV/chloride and UV/H_2O_2, eliminated the estrogenicity of a mixture of bisphenol A, 17β-estradiol, and 17α-ethinylestradiol at a concentration of 100 μg L^{-1}.[18] In another study, the removal of estrogenic activity from a solution of 17β-estradiol and 17α-ethinylestradiol at 37 μM over 300 min was investigated.[73] The electrochemical filter using carbon nanotubes removed 99.1% and 96.3% of the estrogen mixture in ultrapure and wastewater, respectively. In another work, the use of an advanced oxidation process such as chlorination with ultraviolet radiation for the removal of bisphenol A, 17β-estradiol, and 17α-ethinylestradiol demonstrated that by the end of the reaction, no estrogenic intermediates were formed, reducing the estrogenicity of the generated effluents within 5 min of treatment.[17]

3.5 B15ZnO photocatalyst stability

The stability study of the B15ZnO material was evaluated during three cycles of degradation of EDCs (Fig. 8a).

This study showed that the material maintained its degradation capacity for the PPB, BPA, and EE2 mixture over three cycles (PPB: 86.27 to 88.50%, BPA: 72.03 to 72.75%, and complete degradation of EE2 in all three cycles). Additionally, the amount of Zn leached from the catalyst into the solution was determined at each cycle's end to study its photo-corrosion. The Zn content was 11.52, 13.11, and 13.10 mg L^{-1} after the first, second, and third cycles, representing 2.27%, 2.57%, and 2.58% contained in the material. On the other hand, the Zn concentration leached into the solution after the first reuse cycle of ZIF-8-derived ZnO was higher than that of the composite, totaling 16.89 mg L^{-1}, representing 3.38% of the material. This result confirmed that bentonite increased the stability of the bentonite-supported ZnO photocatalyst compared to ZnO. The generated effluent using the ZnO-based photocatalysts was safe for use, as the Zn concentration was below the maximum permissible limit for wastewater discharged into receiving water bodies (20 mg L^{-1}).[74]

The signal intensity of B15ZnO diffractograms throughout the three cycles remains constant (Fig. 7Sa†). Additionally, FTIR spectra of the B15ZnO catalyst after each reuse cycle (Fig. 7Sb†) showed the bands υ(Si–O) and υ(Zn–O) at 1096 and 525 cm^{-1}, respectively, originating from the calcined bentonite and ZIF-8-derived ZnO. This result indicated that the contaminants were not adsorbed on its surface during reuse, allowing for the availability of active sites for the photocatalytic process and the generation of reactive oxygen species.

3.6 Study of reactive oxygen species and charge carriers using B15ZnO

The study with scavengers of reactive oxygen species and charge carriers (Fig. 8b) showed that the radicals $O_2^{\bullet-}$ and h^+ were the main species involved in the degradation of BPA, followed by $HO^\bullet$. For PPB, h^+ and $O_2^{\bullet-}$ radicals were the species that contributed the most during the degradation of the EDCs. For EE2, the primary reactive species were h^+, followed by $HO^\bullet$ and $O_2^{\bullet-}$ radicals. It has been reported that $HO^\bullet$ radicals were the predominant species in the degradation of tetracycline using the CuO/ZnO material derived from ZIF-8 and a 300 W Xe lamp as the light source.[75] The authors also described that $O_2^{\bullet-}$ radicals and h^+ significantly eliminated the antibiotic. In another study, the $O_2^{\bullet-}$ radicals and h^+ were the main species involved in tetracycline elimination using ZnO@In_2O_3 derived from ZIF-8@MIL-68(In).[76] Based on photoluminescence results and studies with scavengers of reactive oxygen species and charge carriers, the following mechanism on the photocatalyst surface is proposed (eqn (2)–(5)).

$$\text{Bentonite/ZnO} + h\nu \rightarrow h^+ + e^- \quad (2)$$

$$(O_2)_{aq} + {e_{CB}}^- \rightarrow O_2^{\bullet-} \xrightarrow{H^+} HO_2^\bullet \xrightarrow{e^-,H^+} H_2O_2 \quad (3)$$

$$H_2O_2 + {e_{CB}}^- \rightarrow HO^\bullet + HO^- \quad (4)$$

$$H_2O + h^+ \rightarrow H^+ + HO^\bullet \quad (5)$$

In the mechanism, the composite is activated with an energy greater than its bandgap, and h^+ were formed in the VB of the material (eqn (2)), which can participate in the degradation of contaminants, such as PPB and EE2. As demonstrated by scavenger studies, the O_2 adsorbed on the semiconductor surface reacted with the e^- accumulated in the material's CB to produce $O_2^{\bullet-}$ (E = −0.33 eV *vs.* NHE). In eqn (3) and (4), the generated $O_2^{\bullet-}$ radicals may react with water to form H_2O_2, which simultaneously breaks down to yield $HO^\bullet$.[77] However, ZnO may have a more positive VB potential than the $HO^\bullet/OH^-$ potential (standard redox potential: +1.99 eV), which would consequently promote the generation of $HO^\bullet$ radicals.[78] Additionally, the h^+ could react with H_2O molecules on the surface of B15ZnO to form $HO^\bullet$ radicals (eqn (5)), which also participate in the degradation of contaminants.[54] However, the contribution of $HO^\bullet$ is negligible (Fig. 8b). Additionally, the oxygen vacancies in B15ZnO trapped the photogenerated e^- in the catalyst, reducing the e^-/h^+ recombination rate in the system. This, in turn, enhanced the photocatalytic efficiency for the degradation of EDCs.[11]

4. Conclusions

The bentonite/ZnO material was synthesized by a microwave-assisted method and calcination at 550 °C in an airflow environment. The resulting bentonite/ZnO composites exhibited reduced crystallite size, increased surface area, carbon/nitrogen dopants, oxygen vacancies, and a decreased recombination rate of e^-/h^+ pairs compared to pure ZnO. Additionally, small amounts of metal oxides (TiO_2, Fe_2O_3, ZnO) in bentonite enhanced the removal of EDCs.

Mineralization was most effective at pH 7 using the B15ZnO composite (61.26%), surpassing the performance of ZIF-8-

derived ZnO (50.94%). The photocatalytic process using B15ZnO produced acetic acid (*m*/*z* 62.02) and lower molecular weight by-products, indicating the breakdown of the hormone EE2's structure. This led to a significant reduction in estrogenic activity without forming estrogenic byproducts, demonstrating its effectiveness.

The B15ZnO catalyst maintained its properties over three cycles of degradation of EDCs. Incorporating bentonite also inhibited photo-corrosion on ZnO's surface. Analysis showed that $O_2^{\bullet-}$ radicals and h^+ were involved in degrading BPA, while h^+ and $O_2^{\bullet-}$ were key in removing PPB. For EE2 degradation, the main reactive species were h^+, followed by $HO^\bullet$ and $O_2^{\bullet-}$ radicals. Thus, the bentonite/ZIF-8-derived ZnO composite is proposed as an alternative ZnO-based catalyst for effectively removing EDCs from aqueous media.

Author contributions

P. C. Quero-Jiménez: methodology, investigation, formal analysis, and writing – original draft. A. Hernández-Ramírez: writing – review & editing, formal analysis and supervision. G. Gomes: investigation, writing – review & editing, methodology, and formal analysis. J. L. Guzmán-Mar: formal analysis, validation, and writing – review & editing. D. Maia-Bila: formal analysis, writing – review & editing, and supervision. L. Hinojosa-Reyes: formal analysis, writing – review & editing, supervision, funding acquisition, and conceptualization.

Data availability

The data supporting this article have been included in the ESI.†

Conflicts of interest

There are no conflicts to declare.

Acknowledgements

This research was supported by Facultad de Ciencias Químicas, UANL, and Ciencia de Frontera 2019-CONAHCyT-Mexico (1727980). The financial assistance from Brazilian governmental institutions FAPERJ (Proc. E-26/010.002251/2019 and Proc. E-26/201.111/2021) and CNPq (Proc. 314471/2021-9) is acknowledged. P. C. Quero-Jiménez thanks CONAHCyT-Mexico for the scholarship (grant number 1022942).

References

1 P. T. Pham, T. C. Quan, Q. T. Le, M. Q. Bui, A. H. Tran, A.-T. T. Phung, A. Q. Hoang, T. B. Minh, T.-T. Tran-Lam, H. N. Tran and T. M. Tran, Quantification of parabens in marine fish samples by a rapid, simple, effective sample preparation method, *Environ. Sci. Pollut. Res.*, 2024, **31**, 16571–16582.

2 A. Grobin, R. Roškar and J. Trontelj, The environmental occurrence, fate, and risks of 25 endocrine disruptors in Slovenian waters, *Sci. Total Environ.*, 2024, **906**, 167245.

3 I. B. De Heredia, B. González-Gaya, O. Zuloaga, I. Garrido, T. Acosta, N. Etxebarria and E. Ruiz-Romera, Occurrence of emerging contaminants in three river basins impacted by wastewater treatment plant effluents: Spatio-seasonal patterns and environmental risk assessment, *Sci. Total Environ.*, 2024, **946**, 174062.

4 M. Durcik, A. Grobin, R. Roškar, J. Trontelj and L. P. Mašič, Estrogenic potency of endocrine disrupting chemicals and their mixtures detected in environmental waters and wastewaters, *Chemosphere*, 2023, **330**, 138712.

5 H. E. Costa and E. Cairrao, Effect of bisphenol A on the neurological system: a review update, *Arch. Toxicol.*, 2024, **98**, 1–73.

6 M. U. Rehman, B. Nisar, A. M. Yatoo, N. Sehar, R. Tomar, L. Tariq, S. Ali, A. Ali, S. M. Rashid, S. B. Ahmad and R. M. Aldossari, After effects of Pharmaceuticals and Personal Care Products (PPCPs) on the biosphere and their counteractive ways, *Sep. Purif. Technol.*, 2024, **342**, 126921.

7 P. M. Gaidhani, S. Chakraborty, K. Ramesh, P. Velayudhaperumal Chellam and E. D. van Hullebusch, Molecular interactions of paraben family of pollutants with embryonic neuronal proteins of *Danio rerio*: A step ahead in computational toxicity towards adverse outcome pathway, *Chemosphere*, 2024, **351**, 141155.

8 G.-Y. Huang, G.-Z. Fang, W.-J. Shi, X.-P. Li, C.-S. Wang, H.-X. Chen, L. Xie and G.-G. Ying, Interaction of 17α-ethinylestradiol and methyltestosterone in western mosquitofish (*Gambusia affinis*) across two generations, *Aquat. Toxicol.*, 2024, **268**, 106854.

9 S. Payra, S. Challagulla, Y. Bobde, C. Chakraborty, B. Ghosh and S. Roy, Probing the photo- and electro-catalytic degradation mechanism of methylene blue dye over ZIF-derived ZnO, *J. Hazard. Mater.*, 2019, **373**, 377–388.

10 A. Faraji, N. Mehrdadi, N. M. Mahmoodi, M. Baghdadi and A. Pardakhti, Enhanced photocatalytic activity by synergic action of ZIF-8 and $NiFe_2O_4$ under visible light irradiation, *J. Mol. Struct.*, 2021, **1223**, 129028.

11 A. Mariappan, P. Mannu, T. Thiruppathiraja, T. T. T. Nga, S. Lakshmipathi, C.-L. Dong, R. K. Dharman and T. H. Oh, Interfacial oxygen vacancy modulated ZIF-8-derived ZnO/CuS for the photocatalytic degradation of antibiotic and organic pollutants: DFT calculation and degradation pathways, *Chem. Eng. J.*, 2023, **476**, 146720.

12 F. Yu, J. Ren, J. Zhang, H. Chen, X. Tian, C. Feng, C. Li, J. Zhang, X. Tang and X. Hou, Structural and optical properties of polyhedral N-doped ZnO@$BiVO_4$ nanocomposite photocatalyst derived from ZIF-8, *Vacuum*, 2024, **220**, 112814.

13 L. L. Zulfa, R. Ediati, A. R. P. Hidayat, R. Subagyo, N. Faaizatunnisa, Y. Kusumawati, D. Hartanto,

N. Widiastuti, W. P. Utomo and M. Santoso, Synergistic effect of modified pore and heterojunction of MOF-derived α-Fe_2O_3/ZnO for superior photocatalytic degradation of methylene blue, *RSC Adv.*, 2023, **13**, 3818–3834.

14 N. Sun, X. Si, L. He, J. Zhang and Y. Sun, Strategies for enhancing the photocatalytic activity of semiconductors, *Int. J. Hydrogen Energy*, 2024, **58**, 1249–1265.

15 K. Kalpana and K. Rajathi, Eco-friendly natural clay bentonite supported zirconium titanate (BT–$ZrTiO_4$): synthesis, characterization and photocatalysis and self-cleaning activities, *J. Mater. Sci.:Mater. Electron.*, 2024, **35**, 187.

16 N. Sheilatina, N. Fathurrahmi, F. Frastiwi, W. I. Nawawi and S. Sabar, Immobilization of TiO_2/bentonite/α-Fe_2O_3 photocatalyst on glass plates and their study on the degradation of indigo carmine dyes, *AIP Conf. Proc.*, 2024, **3082**, 040013.

17 E. M. Saggioro, F. P. Chaves, L. C. Felix, G. Gomes and D. M. Bila, Endocrine disruptor degradation by UV/Chlorine and the impact of their removal on estrogenic activity and toxicity, *Int. J. Photoenergy*, 2019, **2019**, 1–9.

18 F. P. Chaves, G. Gomes, A. Della-Flora, A. Dallegrave, C. Sirtori, E. M. Saggioro and D. M. Bila, Comparative endocrine disrupting compound removal from real wastewater by UV/Cl and UV/H_2O_2: Effect of pH, estrogenic activity, transformation products and toxicity, *Sci. Total Environ.*, 2020, **746**, 141041.

19 S. Al Abdulla, R. Sabouni, M. Ghommem and A. H. Alami, Synthesis and performance analysis of zeolitic imidazolate frameworks for CO_2 sensing applications, *Heliyon*, 2023, **9**, e21349.

20 C. Yang, H. Xu, J. Shi, Z. Liu and L. Zhao, Preparation and photocatalysis of CuO/bentonite based on adsorption and photocatalytic activity, *Materials*, 2021, **14**, 5803.

21 J. I. Langford and A. J. C. Wilson, Scherrer after sixty years: A survey and some new results in the determination of crystallite size, *J. Appl. Crystallogr.*, 1978, **11**, 102–113.

22 E. J. Routledge and J. P. Sumpter, Estrogenic activity of surfactants and some of their degradation products assessed using a recombinant yeast screen, *Environ. Toxicol. Chem.*, 1996, **15**, 241–248.

23 G. Gomes, A. dos S. Argolo, L. da C. Felix and D. M. Bila, Interferences in the yeast estrogen screen (YES) assay for evaluation of estrogenicity in environmental samples, chemical mixtures, and individual substances, *Toxicol. In Vitro*, 2023, **88**, 105551.

24 C. Feng, Z. Chen, J. Jing and J. Hou, The photocatalytic phenol degradation mechanism of Ag-modified ZnO nanorods, *J. Mater. Chem. C*, 2020, **8**, 3000–3009.

25 R. Rameshbabu, G. Pecchi, E. J. Delgado, R. V. Mangalaraja and M. Sathish, Ultrasound-assisted room temperature synthesis of flower-like-Bi_5O_7I-incorporated reduced graphene oxide nanosheets for highly efficient visible-light photocatalytic activity, *J. Phys. Chem. C*, 2020, **124**, 20898–20910.

26 A. Han, H. Zhang, D. Lu, J. Sun, G. K. Chuah and S. Jaenicke, Efficient photodegradation of chlorophenols by BiOBr/$NaBiO_3$ heterojunctioned composites under visible light, *J. Hazard. Mater.*, 2018, **341**, 83–92.

27 R. E. Núñez-Salas, A. Hernández-Ramírez, V. Santos-Lozano, L. Hinojosa-Reyes, J. L. Guzmán-Mar, M. Á. Gracia-Pinilla and M. de L. Maya-Treviño, Synthesis, characterization, and photocatalytic performance of $FeTiO_3$/ZnO on ciprofloxacin degradation, *J. Photochem. Photobiol., A*, 2021, **411**, 113186.

28 K. Li, M. Chen, L. Chen, S. Zhao, W. Pan, P. Li and Y. Han, Adsorption of tetracycline from aqueous solution by ZIF-8: Isotherms, kinetics and thermodynamics, *Environ. Res.*, 2024, **241**, 117588.

29 C. H. Belgacem, N. Missaoui, M. A. H. Khalafalla, G. Bouzid, H. Kahri, A. H. Bashal, A. Dhahri, L. Nouar, F. J. Melendez, M. E. Castro, H. Ghalla and Y. Zhou, Synthesis of ultramicroporous zeolitic imidazolate framework ZIF-8 via solid state method using a minimum amount of deionized water for high greenhouse gas adsorption: A computational modeling, *J. Environ. Chem. Eng.*, 2024, **12**, 112086.

30 M. Pérez-Miana, J. M. Luque-Alled, M. Yahia, Á. Mayoral and J. Coronas, ZIF-8 modified with 2-undecylimidazolate as filler for mixed matrix membranes for CO_2 separation, *J. Mater. Chem. A*, 2024, **12**, 10316–10328.

31 A. K. Mohammed, S. M. Saadoon, Z. T. A. Ali, I. M. Rashid and N. H. A. Sbani, Removal of amoxicillin from contaminated water using modified bentonite as a reactive material, *Heliyon*, 2024, **10**, e24916.

32 M. Hajibeygi, F. Soltani, M. Shabanian, M. Maleki, H. A. Khonakdar and B. Kruppke, Plasticized polyvinyl chloride/melamine–cyanurate modified $Mg(OH)_2$@bentonite nanocomposites; mechanical, thermal, and flame retardant properties, *J. Vinyl Addit. Technol.*, 2024, **30**, 114–129.

33 S. Heydari and M. Moradi, Green synthesis of nanochitosan/bentonite/SnO_2–ZnO bionanocomposite for removal of heavy metal ions and photocatalytic degradation of organic dye, *J. Polym. Environ.*, 2024, **32**, 3698–3717.

34 S. Silvestri and E. L. Foletto, Preparation and characterization of Fe_2O_3/TiO_2/clay plates and their use as photocatalysts, *Ceram. Int.*, 2017, **43**, 14057–14062.

35 A. H. Bashal, J. Dhahri, K. Dhahri, H. Ouni and M. Khalafalla, Enhancing dielectric properties of bentonite with Ce and Zn: structural insights and industrial applications, *J. Sol-Gel Sci. Technol.*, 2024, **110**, 473–488.

36 P. C. Quero-Jiménez, L. a. A. Felipe, J. O. P. García, M. E. J. Rodríguez, J. B. de la Torre López, O. N. Montenegro, R. M. Ruiz and I. S. Tiscornia, Local Cuban bentonite clay: composition, structure and textural characterization, *Andean Geol.*, 2021, **48**, 546.

37 M. R. Karim, A. Mohammad, C. B. Mukta, J. Lee and T. Yoon, Biofilm-engineered fabrication of Ag nanoparticles with modified ZIF-8-derived ZnO for a high-performance supercapacitor, *J. Energy Storage*, 2024, **75**, 109646.

38 S. Chávez-Cruz, M. J. Gallegos-Gómora, R. Armijo-Torres, M. A. Guzmán-Cruz, R. Falconi-Calderón and M. Acosta-Alejandro, Archaeometric study of Maya pottery from Comalcalco, Tabasco, Mexico, *J. Archaeol. Sci. Rep.*, 2024, **54**, 104458.

39 B. Yan, S. Liu, M. L. Chastain, S. Yang and J. Chen, A new FTIR method for estimating the firing temperature of ceramic bronze-casting moulds from early China, *Sci. Rep.*, 2021, **11**, 3316.
40 J. Ran, H. Chen, S. Bi, Q. Guo, Z. Deng, G. Cai, D. Cheng, X. Tang and X. Wang, One-step in-situ growth of zeolitic imidazole frameworks-8 on cotton fabrics for photocatalysis and antimicrobial activity, *Cellulose*, 2020, **27**, 10447–10459.
41 P. Behera, A. Ray, S. P. Tripathy, L. Acharya, S. Subudhi and K. Parida, ZIF-8 derived porous C, N co-doped ZnO modified B-g-C_3N_4: A Z-Scheme charge dynamics approach operative towards photocatalytic hydrogen evolution and ciprofloxacin degradation, *J. Photochem. Photobiol., A*, 2023, **436**, 114415.
42 M. M. Bouhent, K. Bentaleb, A. Al-Ameri and U. Maschke, Performance of Mg/Al and Zn/Al hydroxide double lamellar-bentonite for removal of anionic azo dye from aqueous solution, *Processes*, 2024, **12**, 677.
43 M. Yi, H. Li, D. Huang, W. Liu, M. Zhao, X. Tan, Q. Cheng, Q. Ding, Y. Ren, B. Li, G. Han and G. Liu, ZIF-8-derived ZnO doped with In for high-performance ethanol gas sensor, *J. Mater. Sci.:Mater. Electron.*, 2024, **35**, 342.
44 M. Jian, B. Liu, G. Zhang, R. Liu and X. Zhang, Adsorptive removal of arsenic from aqueous solution by zeolitic imidazolate framework-8 (ZIF-8) nanoparticles, *Colloids Surf., A*, 2015, **465**, 67–76.
45 N. Talukder, Y. Wang, B. B. Nunna, X. Tong and E. S. Lee, An investigation on the structural stability of ZIF-8 in water versus water-derived oxidative species in aqueous environment, *Microporous Mesoporous Mater.*, 2024, **366**, 112934.
46 H. Zhang, M. Zhao, Y. Yang and Y. S. Lin, Hydrolysis and condensation of ZIF-8 in water, *Microporous Mesoporous Mater.*, 2019, **288**, 109568.
47 M. Liang, Y. Yan, J. Yang, X. Liu, R. Jia, Y. Ge, Z. Li and L. Huang, *In situ*-derived N-doped ZnO from ZIF-8 for enhanced ethanol sensing in ZnO/MEMS devices, *Molecules*, 2024, **29**, 1703.
48 R. Wang, H. Dong, X. Li, L. Zhou, W. Zhu and T. Chen, Biomass encapsulated ZIF-8-derived ZnO carbon aerogels for efficient uranium extraction by synergistic adsorption-photoreduction, *Chem. Eng. J.*, 2023, **478**, 147331.
49 Y. Yin, J. Liu, Z. Wu, T. Zhang and Z. Li, ZIF-8 calcination derived Cu_2O–ZnO* material for enhanced visible-light photocatalytic performance, *New J. Chem.*, 2021, **45**, 3095–3101.
50 Z. Zhang, Y. Chen, C. Hu, C. Zuo, P. Wang, W. Chen and T. Ao, Efficient removal of tetracycline by a hierarchically porous ZIF-8 metal organic framework, *Environ. Res.*, 2021, **198**, 111254.
51 J. Cheng, R. Gu, P. He, Y. Pan, Y. Leng, Y. Wang, Y. Liu, M. Zhu and X. Tuo, Effect of high-dose γ-ray irradiation on the structural stability and U(VI) adsorption ability of bentonite, *J. Radioanal. Nucl. Chem.*, 2022, **331**, 339–352.
52 B. Joshi, S. Kim, E. Samuel, J. Huh, A. Aldalbahi, M. Rahaman, B. Ding and S. S. Yoon, ZIF-8-derived hierarchical ZnO nanoplates anchored to low-density carbon fabric: Highly flexible supercapacitors with wide potential windows, *J. Power Sources*, 2024, **604**, 234463.
53 Y. Wang, Y. Kang, Y. Miao, M. Jia, S. Long, L. Diao, L. Zhang, D. Li and G. Wu, S-dopant and O-vacancy of mesoporous ZnO nanosheets induce high efficiency and selectivity of electrocatalytic CO_2 reduction to CO, *Compos. Commun.*, 2024, **48**, 101890.
54 M. Bai, R. Chen, X. Liu, H. Li, J. Li, H. Huang, M. Song, Q. Zhang, Y. Su, H. Wang, M. Xu and G. Xie, An effective strategy for synthesizing high-performance photocatalyst by recycling the graphite target wastes, *J. Environ. Chem. Eng.*, 2024, **12**, 113872.
55 A. I. A. Soliman, A.-M. A. Abdel-Wahab and H. N. Abdelhamid, Hierarchical porous zeolitic imidazolate frameworks (ZIF-8) and ZnO@N-doped carbon for selective adsorption and photocatalytic degradation of organic pollutants, *RSC Adv.*, 2022, **12**, 7075–7084.
56 J. Wang, W. Wang, Z. Ai, M. Li, H. Li, W. Peng, Y. Zhao and S. Song, Adsorption toward Pb(II) occurring on three-dimensional reticular-structured montmorillonite hydrogel surface, *Appl. Clay Sci.*, 2021, **210**, 106153.
57 L. Pan, T. Muhammad, L. Ma, Z.-F. Huang, S. Wang, L. Wang, J.-J. Zou and X. Zhang, MOF-derived C-doped ZnO prepared via a two-step calcination for efficient photocatalysis, *Appl. Catal., B*, 2016, **189**, 181–191.
58 T. T. B. Dao, L. T. T. Ha, N. H. Le, D. T. Nguyen, T. H. Nguyen and C.-N. Ha-Thuc, characterization and the effect of different parameters on photocatalytic activity of montmorillonite/TiO_2 nanocomposite under UVC irradiation, *Period. Polytech., Chem. Eng.*, 2024, **68**, 35–49.
59 Q. Zhang, G. Xie, M. Duan, Y. Liu, Y. Cai, M. Xu, K. Zhao, H. Tai, Y. Jiang and Y. Su, Zinc oxide nanorods for light-activated gas sensing and photocatalytic applications, *ACS Appl. Nano Mater.*, 2023, **6**, 17445–17456.
60 M. Hu, D. Zhao, X. Yan, X. Hu, M. Zhou, Y. Shu and P. Liu, Construction of Z-scheme heterojunction ZIF-8-decorated ZnO/SiO_2 for enhanced visible-light photocatalytic removal of organic pollutants and reduction of Cr(VI), *Appl. Surf. Sci.*, 2024, **665**, 160321.
61 A. H. Zyoud, A. Zubi, S. H. Zyoud, M. H. Hilal, S. Zyoud, N. Qamhieh, A. Hajamohideen and H. S. Hilal, Kaolin-supported ZnO nanoparticle catalysts in self-sensitized tetracycline photodegradation: Zero-point charge and pH effects, *Appl. Clay Sci.*, 2019, **182**, 105294.
62 M. Kıranşan, A. Khataee, S. Karaca and M. Sheydaei, Artificial neural network modeling of photocatalytic removal of a disperse dye using synthesized of ZnO nanoparticles on montmorillonite, *Spectrochim. Acta, Part A*, 2015, **140**, 465–473.
63 A. Khataee, A. Karimi, S. Arefi-Oskoui, R. D. C. Soltani, Y. Hanifehpour, B. Soltani and S. W. Joo, Sonochemical synthesis of Pr-doped ZnO nanoparticles for sonocatalytic degradation of Acid Red 17, *Ultrason. Sonochem.*, 2014, **22**, 371–381.

64 S. G. Anju, S. Yesodharan and E. P. Yesodharan, Zinc oxide mediated sonophotocatalytic degradation of phenol in water, *Chem. Eng. J.*, 2012, **189–190**, 84–93.
65 K. Selvakumar, A. Raja, M. Arunpandian, K. Stalindurai, P. Rajasekaran, P. Sami, E. R. Nagarajan and M. Swaminathan, Efficient photocatalytic degradation of ciprofloxacin and bisphenol A under visible light using Gd_2WO_6 loaded ZnO/bentonite nanocomposite, *Appl. Surf. Sci.*, 2019, **481**, 1109–1119.
66 D. A. Pino-Sandoval, L. Hinojosa-Reyes, J. L. Guzmán-Mar, J. C. Murillo-Sierra and A. Hernández-Ramírez, Solar photocatalysis for degradation of pharmaceuticals in hospital wastewater: Influence of the type of catalyst, aqueous matrix, and toxicity evaluation, *Water, Air, Soil Pollut.*, 2022, **233**, 14.
67 Y. Lin, C. Ferronato, N. Deng, F. Wu and J.-M. Chovelon, Photocatalytic degradation of methylparaben by TiO_2: Multivariable experimental design and mechanism, *Appl. Catal., B*, 2009, **88**, 32–41.
68 P. C. Quero-Jiménez, A. Hernández-Ramírez, J. L. Guzmán-Mar, M. Villanueva-Rodríguez, D. A. Pino-Sandoval and L. Hinojosa-Reyes, Applicability of NH_2-MOF235(Fe)-derived α-Fe_2O_3/ZnO photocatalyst synthesized by the microwave-assisted method in the degradation of a mixture of phenolic compounds, *J. Photochem. Photobiol., A*, 2024, **446**, 115154.
69 T. Geng, C. Yi, R. Yi, L. Yang and M. I. Nawaz, Mechanism and degradation pathways of Bisphenol A in aqueous solution by strong ionization discharge, *Water, Air, Soil Pollut.*, 2020, **231**, 185.
70 N. G. Menon, L. George, S. S. V. Tatiparti and S. Mukherji, Efficacy and reusability of mixed-phase TiO_2–ZnO nanocomposites for the removal of estrogenic effects of 17β-Estradiol and 17α-Ethinylestradiol from water, *J. Environ. Manage.*, 2021, **288**, 112340.
71 E. Priyadarshini, A. M. Parambil, P. Rajamani, V. K. Ponnusamy and Y.-H. Chen, Exposure, toxicological mechanism of endocrine disrupting compounds and future direction of identification using nano-architectonics, *Environ. Res.*, 2023, **225**, 115577.
72 A. Nadal, A. B. Ropero, O. Laribi, M. Maillet, E. Fuentes and B. Soria, Nongenomic actions of estrogens and xenoestrogens by binding at a plasma membrane receptor unrelated to estrogen receptor α and estrogen receptor β, *Proc. Natl. Acad. Sci. U. S. A.*, 2000, **97**, 11603–11608.
73 G. dos S. Cunha, B. M. de Souza-Chaves, D. M. Bila, J. P. Bassin, C. D. Vecitis and M. Dezotti, Insights into estrogenic activity removal using carbon nanotube electrochemical filter, *Sci. Total Environ.*, 2019, **678**, 448–456.
74 SEMARNAT, Norma Oficial Mexicana NOM-001-SEMARNAT-2021, que establece los límites permisibles de contaminantes en las descargas de aguas residuales en cuerpos receptores propiedad de la nación, *Secretaría de Medio Ambiente y Recursos Naturales., Diario Oficial de la Federación*, 2021.
75 X. Lei, Y. Cao, Q. Chen, X. Ao, Y. Fang and B. Liu, ZIF-8 derived hollow CuO/ZnO material for study of enhanced photocatalytic performance, *Colloids Surf., A*, 2019, **568**, 1–10.
76 J. Li, L. Liu, Q. Liang, M. Zhou, C. Yao, S. Xu and Z. Li, Core-shell ZIF-8@MIL-68(In) derived ZnO nanoparticles-embedded In2O3 hollow tubular with oxygen vacancy for photocatalytic degradation of antibiotic pollutant, *J. Hazard. Mater.*, 2021, **414**, 125395.
77 J. Schneider, M. Matsuoka, M. Takeuchi, J. Zhang, Y. Horiuchi, M. Anpo and D. W. Bahnemann, Understanding TiO_2 Photocatalysis: Mechanisms and materials, *Chem. Rev.*, 2014, **114**, 9919–9986.
78 F. Chang, W. Yan, X. Wang, S. Peng, S. Li and X. Hu, Strengthened photocatalytic removal of bisphenol a by robust 3D hierarchical n-p heterojunctions $Bi_4O_5Br_2$-MnO_2 via boosting oxidative radicals generation, *Chem. Eng. J.*, 2022, **428**, 131223.